Higgs to four leptons

Matteo Malucchi

June 2022

1 Introduction

The Higgs boson was discovered in 2012 by the ATLAS [1] and CMS [2] experiments at LHC at CERN. Since the discovery, many properties of this new particle were studied, in particular its spin and parity quantum numbers. In the Standard Model (SM), the Higgs boson has $J^P = 0^+$ and the several studies indicate the compatibility with this prediction, as described in Refs. [3] [4]. Particularly, the hypothesis $J^P = 0^+$ has been compared to alternative models, including a pseudoscalar boson $J^P = 0^-$ and a graviton-like boson $J^P = 2^+$, which have been excluded at 99.9 % CL in favour of the SM hypothesis. In this report it will be analyzed exclusively the channel $H \to ZZ^* \to 4l$ using data from the ATLAS experiment. In particular the main focus will be on the p_T, η, φ and invariant mass distributions of the various particles, whilst also concentrating on the five angles defined in [5] which allow to determine the spin-parity of the boson.

2 Dataset

The samples of data, as well as the Monte Carlo (MC) simulations, used for this analysis can be found at ATLAS open data. The data has been collected by the ATLAS detector at 13 TeV during the year 2016 and corresponds to an integrated luminosity $\mathcal{L} = 10.06 \pm 0.37$ fb^{-1}. The collision data is accompanied by a set of MC simulated samples describing the processes which are used to model the expected distributions of signal and background events. The main features of the data and the MC samples are summarized in Tables 1 and 2 respectively.

Data sample	Number of events
data_A.4lep	39
data_B.4lep	156
data_C.4lep	237
data_D.4lep	400

Table 1: Description of the data samples containing four leptons released in the 13 TeV ATLAS Open Data.

2.1 Normalization of the histograms

The total number of expected events for a process generated with a MC simulation is

$$n_{events} = \mathcal{L}\,\sigma$$

where σ is the cross section of such process. The events from MC samples are associated with the weight

$$w = \texttt{mc\_Weight} \cdot \texttt{scaleFactor\_ELE} \cdot \texttt{scaleFactor\_MUON} \cdot \texttt{scaleFactor\_LepTRIGGER} \cdot \texttt{scaleFactor\_PILEUP}$$

which is used to fill the histograms. The content of the i-th bin is the sum of the weights of the events in that bin

$$BinContent_i = \sum_{bin_i} w$$

The probability of an event to be in the i-th bin is

$$p_i = \frac{BinContent_i}{\sum w}$$

where $\sum w$ is the sum of the weights over all bins (reported in Figure 2). So the expected number of events in the i-th bin is

$$n_i = \mathcal{L}\,\sigma\,\frac{BinContent_i}{\sum w}$$

Process	Unique "channel number"	Number of events	Cross section [pb]	Sum of weights	Generator
W/Z (+jets) production					
$Z \to e^+e^-$	361106	898	1950.5295	150277594200	POWHEG-BOX v2 + PYTHIA 8
$Z \to \mu^+\mu^-$	361107	684	1950.6321	147334691090	POWHEG-BOX v2 + PYTHIA 8
$Z \to \tau^+\tau^-$	361108	9	1950.6321	56171652547.3	POWHEG-BOX v2 + PYTHIA 8
$W^+ \to e^+\nu_e$	361100	41502	11500.4632	473389396815	POWHEG-BOX v2 + PYTHIA 8
$W^+ \to \mu^+\nu_\mu$	361101	35184	11500.4632	446507925520	POWHEG-BOX v2 + PYTHIA 8
$W^+ \to \tau^+\nu_\tau$	361102	1774	11500.4632	670928468875	POWHEG-BOX v2 + PYTHIA 8
$W^- \to e^-\bar{\nu}_e$	361103	31893	8579.63498	247538642447	POWHEG-BOX v2 + PYTHIA 8
$W^- \to \mu^-\bar{\nu}_\mu$	361104	30307	8579.63498	264338188182	POWHEG-BOX v2 + PYTHIA 8
$W^- \to \tau^-\bar{\nu}_\tau$	361105	1409	8579.63498	165195850954	POWHEG-BOX v2 + PYTHIA 8
Diboson production					
$ZZ \to qq'l^+l^-$	363356	254	2.20355112	3439266.11559	SHERPA 2.2
$WZ \to qq'l^+l^-$	363358	1316619	3.4328	241438.72705	SHERPA 2.2
$W^+W^- \to qq'l^-\bar{\nu}$	363359	13375	24.7088	998250.783475	SHERPA 2.2
$W^+W^- \to l^+\nu qq'$	363360	14245	24.724	1069526.41899	SHERPA 2.2
$WZ \to l\nu qq'$	363489	28199	11.42	1111991.15979	SHERPA 2.2
$ZZ \to l^+l^-l'^+l'^-$	363490	554279	1.2578	7538705.8077	SHERPA 2.2
$WZ \to l\nu l^+l^-$	363491	9340	4.6049	5441475.00407	SHERPA 2.2
$ZZ \to l^+l^-\nu\bar{\nu}$	363492	137	12.466	5039259.9696	SHERPA 2.2
$WZ \to l\nu\nu\bar{\nu}$	363493	11789	3.2286	1727991.07441	SHERPA 2.2
Top-quark production					
$t\bar{t} + jets$ (1l or 2l)	410000	1031	452.693559	49386600	POWHEG-BOX v2 + PYTHIA 8
single top t-chan	410011	2	44.152	4986200	POWHEG-BOX v1 + PYTHIA 6
single anti-top t-chan	410012	2	26.276	4989800	POWHEG-BOX v1 + PYTHIA 6
single top s-chan	410025	2	2.06121	997800	POWHEG-BOX v2 + PYTHIA 6
single anti-top s-chan	410026	2	1.288662	995400	POWHEG-BOX v2 + PYTHIA 6
single top Wt-chan	410013	2	35.845486	4865800	POWHEG-BOX v2 + PYTHIA 6
single anti-top Wt-chan	410014	2	35.824406	4945600	POWHEG-BOX v2 + PYTHIA 6
SM Higgs production ($m_H = 125$ GeV)					
ggF, $H \to ZZ \to 4l$	345060	164716	0.0060239	27881776.6536	POWHEG-BOX v2 + PYTHIA 8
ZH, $H \to ZZ \to 4l$	341947	14485	0.0000021424784	150000	PYTHIA 8
WH, $H \to ZZ \to 4l$	341964	15379	0.0003769	149400	PYTHIA 8
VBF, $H \to ZZ \to 4l$	344235	191126	0.0004633012	3680490.83243	POWHEG-BOX v2 + PYTHIA 8

Table 2: Description of the MC samples released in the 13 TeV ATLAS Open Data.

3 Object selection

In order to be considered a *good* lepton candidate, the electron or muon must[1]:

- satisfy $p_T > 7$ GeV for electrons ($p_T > 5$ GeV for muons)
- be measured in the pseudorapidity range $|\eta| < 2.47$ for electrons ($|\eta| < 2.5$ for muons)
- be isolated in the tracking detector (reducing the jets misidentified as leptons), meaning that the ratio between the scalar sum of track p_T in a cone of $\Delta R = 0.3$ around the lepton, excluding the lepton track, and the lepton p_T itself is less than 0.30
- be isolated in the calorimeter (also reducing the jets faking leptons), meaning that the ratio between the scalar sum of track E_T in a cone of $\Delta R = 0.2$ around the lepton, excluding the lepton track, and the lepton p_T itself is less than 0.30
- originate from the primary vertex (p.v.), meaning that the absolute value of the z-coordinate of the track wrt. the p.v. z_0 multiplied by $\sin\theta < 0.5$ mm and the absolute value of the ratio between the distance of the track at point of closest approach (p.c.a.) d_0 and its significance < 5 for electrons (< 3 for muons).

In Figure 1 the distributions of the two isolation variables before and after the selection are plotted.
On the other hand, Small-R[2] jets are considered *good* candidates if they satisfy:

- $p_T > 30$ GeV

[1]ATLAS uses a right-handed coordinate system with its origin at the nominal interaction point (IP) in the centre of the detector. The positive x-axis is defined by the direction from the IP to the center of the LHC ring, with the positive y-axis pointing upwards, while the beam direction defines the z-axis. Cylindrical coordinates (r,φ) are used in the transverse plane, being φ the azimuthal angle around the z-axis. The pseudorapidity η is defined in terms of the polar angle θ by $\eta = -\ln\tan(\theta/2)$. The angular distance is defined as $\Delta R = \sqrt{(\Delta\eta)^2 + (\Delta\varphi)^2}$. Transverse momentum and energy are defined as $p_T = p\sin\theta$ and $E_T = E\sin\theta$, respectively.

[2]R is the radius parameter used in the jet reconstruction algorithm.

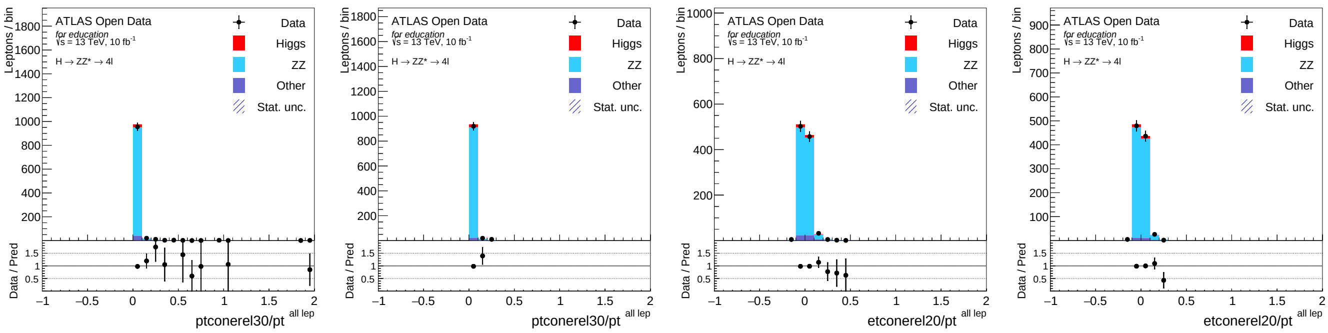

(a) $pt\,cone\,rel\,30/p_T$ no selection (b) $pt\,cone\,rel\,30/p_T < 0.30$ (c) $et\,cone\,rel\,30/p_T$ no selection (d) $et\,cone\,rel\,30/p_T < 0.30$

Figure 1: Distribution before and after the selection of $pt\,cone\,rel\,30/p_T$ and $et\,cone\,rel\,30/p_T$ in the ***4l*** region (see Section 4).

- $|\eta| < 4.4$

From now on *good* leptons (jets) will be referred to as simply leptons (jets). The preselection requirements and object selection for each particle used in this analysis are schematized in Table 3.

Electron	Muon	Small-R jets
InDet & EMCAL rec.	InDet & MS rec.	EMCAL & HCAL rec.
loose identification	loose identification	
loose isolation	loose isolation	
$p_T > 7GeV$	$p_T > 5GeV$	$p_T > 30GeV$
$\|\eta\| < 2.47$	$\|\eta\| < 2.5$	$\|\eta\| < 4.4$
$pt\,cone\,rel\,30/p_T < 0.30$	$pt\,cone\,rel\,30/p_T < 0.30$	anti-k_t jet algorithm, R=0.4
$et\,cone\,rel\,20/p_T < 0.30$	$et\,cone\,rel\,20/p_T < 0.30$	
$\|z_0 \cdot \sin\theta\| < 0.5$ mm	$\|z_0 \cdot \sin\theta\| < 0.5$ mm	
$\|d_0/\sigma_0\| < 5$	$\|d_0/\sigma_0\| < 3$	

Table 3: Preselection requirements and object selection for electron, muon and small-R jets. InDet indicates the inner tracking detector, EMCAL the electro-magnetic calorimeter, HCAL the hadronic calorimeter and MS the muon spectrometer. Reconstruction (rec.), identification, isolation and jet algorithm are given in Refs. [6], [7], [8]

4 Event selection and definition of regions

The event selection requires that either single-electron or single-muon trigger is satisfied. The first lepton with highest p_T is requested to have $p_T > 25$ GeV, the second to have $p_T > 15$ GeV and the third one to have $p_T > 10$ GeV. The leptons are ordered depending on their p_T and therefore are called leptons 1 (highest p_T), 2, 3, 4 (lowest p_T).

The leading Z boson candidate is reconstructed by considering, of all the possible combinations of same-flavor opposite-sign (SFOS) lepton pairs, the one that have mass closest to $m_Z = 91.18$ GeV. This is called leading lepton pair ($ll1$) and the *on-shell* Z boson associated with it is referred to as Z_1. The other *off-shell* Z boson is reconstructed using the remaining SFOS pair ($ll2$) and is called Z_2. The invariant mass of the i-th lepton pair is referred to as m_{lli} and the requirements in all regions but the ones named ***_no_m_lim*** are that 50 GeV $< m_{ll1} <$ 106 GeV and 12 GeV $< m_{ll2} <$ 115 GeV. Subsequently, the Higgs candidate is reconstructed by considering the Z bosons pair. In the regions named ***_m4l_lim*** another requirement is that the invariant mass of the $4l$ system satisfies 115 GeV $< m_{4l} <$ 130 GeV.

The analysis is performed in multiple regions, each containing 4 leptons (e or μ) the charge sum of which is equal to zero. In particular, the regions are defined as follows:

- ***4l*** contains 4 leptons ($e^+e^-e^+e^-$ / $\mu^+\mu^-\mu^+\mu^-$ / $e^+e^-\mu^+\mu^-$) and any number of jets
- ***4e*** contains 4 electrons ($e^+e^-e^+e^-$) and any number of jets
- ***4μ*** contains 4 muons ($\mu^+\mu^-\mu^+\mu^-$) and any number of jets
- ***2e2μ*** contains 2 electrons, 2 muons ($e^+e^-\mu^+\mu^-$) and any number of jets

- ***eeμμ*** contains 2 electrons that form Z_1, 2 muons that form Z_2 ($Z_1Z_2 \to e^+e^-\mu^+\mu^-$) and any number of jets
- ***μμee*** contains 2 muons that form Z_1, 2 electrons that form Z_2 ($Z_1Z_2 \to \mu^+\mu^-e^+e^-$) and any number of jets
- $\boldsymbol{4l + 0jets}$ contains 4 leptons and 0 jets
- $\boldsymbol{4l + 1jets}$ contains 4 leptons and 1 jet
- $\boldsymbol{4l + 2jets}$ contains 4 leptons and 2 jets
- ***4l_no_m_lim*** contains 4 leptons ($e^+e^-e^+e^-$ / $\mu^+\mu^-\mu^+\mu^-$ / $e^+e^-\mu^+\mu^-$), any number of jets and doesn't require any constraints on m_{lli}
- ***4e_no_m_lim*** contains 4 electrons ($e^+e^-e^+e^-$), any number of jets and doesn't require any constraints on m_{lli}
- ***4μ_no_m_lim*** contains 4 muons ($\mu^+\mu^-\mu^+\mu^-$), any number of jets and doesn't require any constraints on m_{lli}
- ***eeμμ_no_m_lim*** contains 2 electrons that form Z_1, 2 muons that form Z_2 ($Z_1Z_2 \to e^+e^-\mu^+\mu^-$), any number of jets and doesn't require any constraints on m_{lli}
- ***μμee_no_m_lim*** contains 2 muons that form Z_1, 2 electrons that form Z_2 ($Z_1Z_2 \to \mu^+\mu^-e^+e^-$), any number of jets and doesn't require any constraints on m_{lli}
- ***4l_m4l_lim*** contains 4 leptons ($e^+e^-e^+e^-$ / $\mu^+\mu^-\mu^+\mu^-$ / $e^+e^-\mu^+\mu^-$), any number of jets and requires a constraint on m_{4l}

A summary of the requirements for each region can be found in Table 4.

5 Results

For each region defined above, *lepton*, *jet*, *global* and *spin-parity* variables were defined and their distributions were plotted[3].

- The *lepton* variables are the ones regarding a single electron or muon, they can be plotted separately for each lepton in the event or can be combined in a single inclusive plot where each event is considered four times, once for each lepton. This variables are the transverse momentum p_T, energy E, pseudorapidity η, azimuthal angle φ, calorimetric isolation $et\,cone\,rel\,20/p_T$, tracking detector isolation $pt\,cone\,rel\,30/p_T$, distance wrt. the p.v. $z_0 \cdot \sin\theta$, significance of the track at p.c.a. d_0/σ_0, charge of the leptons Q, lepton type $|PDG\ ID|$ ($e = 11$, $\mu = 13$).
- The *jet* variables concern the jet candidates and are the p_T, η, φ of the jet 1, 2, 3 (in descending p_T order). In this category there is also the total number of jets in the event.
- The *global* variables are the ones concerning the objects reconstructed starting from the leptons (i.e. Z_1, Z_2, Higgs boson candidates). In particular, the variables are the p_T, η, φ and invariant mass of $ll1$, $ll2$ and $4l$ systems.
- The *spin-parity* variables are the five angles which allow to determine the spin-parity of the Higgs boson described in detail in Section 5.4.

In each of the following plots the points represent experimental data and the filled histograms show the prediction from different MC of the SM Higgs, the main irreducible background of non-resonant ZZ and minor reducible background processes, denoted by "Other", which are primarily $t\bar{t}$, $Z + jets$, $W + jets$ and single-top quark, where lepton candidates arise either from decays of hadrons with $b-$ or $c-$quark content or from misidentification of jets. The contributions are stacked. The statistical uncertainty is represented by the error bars on the data points and the hashed area on the MC prediction.

5.1 *Lepton* variables

In Figure 2 the *lepton* variables in the $\boldsymbol{4l}$ region for the four leptons combined are plotted. The distributions in η are concentrated around 0 since it is in that phase space region that the relevant processes take place. On the contrary, the φ distributions are uniform because the system has cylindrical symmetry around the z-axis. The calorimetric and tracking isolation distributions are concentrated around 0 being the leptons from the examined processes produced far from each other. The small contaminations above and below zero may be caused by detector effects or other particles near the lepton in consideration, in any case they are well predicted by MC simulations. The number of positive leptons is equal to the negative one because the events were selected with this request. Furthermore, the number of

[3] Since over a thousand plots were created, not all them are shown in this report. The complete set can be found in this repository.

Lepton p_T	Trigger	Charge sum
$p_{T,l1} > 25$ GeV $p_{T,l2} > 15$ GeV $p_{T,l3} > 10$ GeV	`trigE || trigM`	0

Region	Leptons	Small-R jets	Mass constraints
$\boldsymbol{4l}$	$e^+e^-e^+e^-$ / $\mu^+\mu^-\mu^+\mu^-$ / $e^+e^-\mu^+\mu^-$	any	50 GeV $< m_{ll1} <$ 106 GeV 12 GeV $< m_{ll2} <$ 115 GeV
$\boldsymbol{4e}$	$e^+e^-e^+e^-$	any	50 GeV $< m_{ll1} <$ 106 GeV 12 GeV $< m_{ll2} <$ 115 GeV
$\boldsymbol{4\mu}$	$\mu^+\mu^-\mu^+\mu^-$	any	50 GeV $< m_{ll1} <$ 106 GeV 12 GeV $< m_{ll2} <$ 115 GeV
$\boldsymbol{2e2\mu}$	$e^+e^-\mu^+\mu^-$	any	50 GeV $< m_{ll1} <$ 106 GeV 12 GeV $< m_{ll2} <$ 115 GeV
$\boldsymbol{ee\mu\mu}$	$Z_1Z_2 \to e^+e^-\mu^+\mu^-$	any	50 GeV $< m_{ll1} <$ 106 GeV 12 GeV $< m_{ll2} <$ 115 GeV
$\boldsymbol{\mu\mu ee}$	$Z_1Z_2 \to \mu^+\mu^-e^+e^-$	any	50 GeV $< m_{ll1} <$ 106 GeV 12 GeV $< m_{ll2} <$ 115 GeV
$\boldsymbol{4l+0jets}$	$e^+e^-e^+e^-$ / $\mu^+\mu^-\mu^+\mu^-$ / $e^+e^-\mu^+\mu^-$	0	50 GeV $< m_{ll1} <$ 106 GeV 12 GeV $< m_{ll2} <$ 115 GeV
$\boldsymbol{4l+1jets}$	$e^+e^-e^+e^-$ / $\mu^+\mu^-\mu^+\mu^-$ / $e^+e^-\mu^+\mu^-$	1	50 GeV $< m_{ll1} <$ 106 GeV 12 GeV $< m_{ll2} <$ 115 GeV
$\boldsymbol{4l+2jets}$	$e^+e^-e^+e^-$ / $\mu^+\mu^-\mu^+\mu^-$ / $e^+e^-\mu^+\mu^-$	2	50 GeV $< m_{ll1} <$ 106 GeV 12 GeV $< m_{ll2} <$ 115 GeV
4l_no_m_lim	$e^+e^-e^+e^-$ / $\mu^+\mu^-\mu^+\mu^-$ / $e^+e^-\mu^+\mu^-$	any	none
4e_no_m_lim	$e^+e^-e^+e^-$	any	none
4μ_no_m_lim	$\mu^+\mu^-\mu^+\mu^-$	any	none
eeμμ_no_m_lim	$Z_1Z_2 \to e^+e^-\mu^+\mu^-$	any	none
μμee_no_m_lim	$Z_1Z_2 \to \mu^+\mu^-e^+e^-$	any	none
4l_m4l_lim	$e^+e^-e^+e^-$ / $\mu^+\mu^-\mu^+\mu^-$ / $e^+e^-\mu^+\mu^-$	any	50 GeV $< m_{ll1} <$ 106 GeV 12 GeV $< m_{ll2} <$ 115 GeV 115 GeV $< m_{4l} <$ 130 GeV

Table 4: Definition of the regions. Lepton p_T, Trigger and Charge sum requirements are common to all regions, while in the inferior section of the table the requirements for the specific region are indicated.

electrons is compatible with the number of muons within one standard deviation. This is what to expect because the branching fraction of Z in e^+e^- is approximately equal to the one of Z in $\mu^+\mu^-$. Apart from the two variables that assure that the lepton originated from the p.v., there is a *good* agreement between data and MC.

In Figure 3 the distributions in p_T and E for leptons 1, 2, 3 and 4 in the $\boldsymbol{4l}$ region are shown. As expected, the only qualitative differences between the distributions of all the four leptons combined and the ones of the leptons taken separately consist in the distributions of p_T and E. In fact, the distributions for lepton 1 tend towards higher values, while the ones for lepton 4 peak in zero.

5.2 *Jet* variables

In Figure 4 the *jet* variables in the $\boldsymbol{4l}$ region are plotted. The distributions of jets 1, 2 and 3 have decreasing statistics because, as shown in Figure 4a, the number of events with a single jet is roughly 4 times the one with three jets. As expected, the p_T distribution of jet 1 is concentrated at higher values respect to the distribution of jet 3. Again, the φ distributions are uniform (cylindrical symmetry) while the η ones are concentrated around zero. However, in contrast to the η plot for the leptons in Figure 2, in this case the distributions seem to be more *flat*. This may be caused by the fact that the jets originate not only from processes which yield high-θ decay products but also from partons which scatter at low angles and cause the flattening of the distributions. This can be seen also in Figure 5, where the η distributions in the $\boldsymbol{4l+1jet}$ region are plotted. In this case, the distributions have the same statistics and the pattern observed before can be seen here too. There is generally a *good* agreement between data and MC simulations.

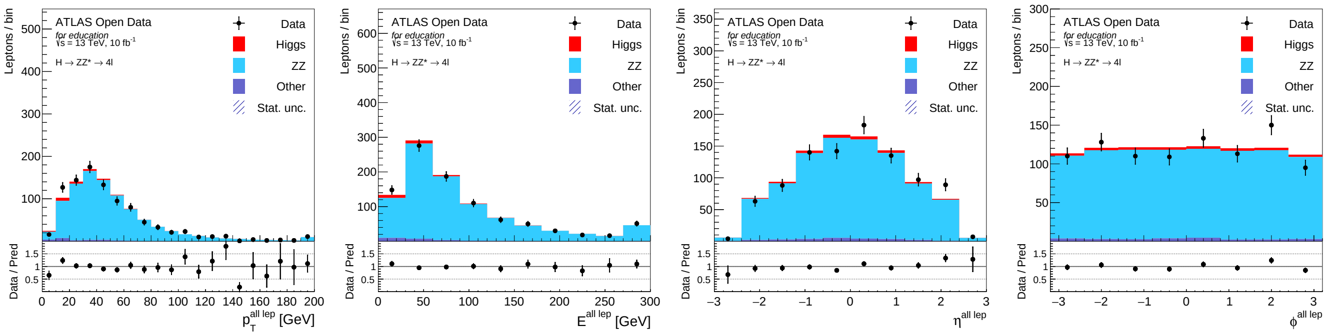

(a) Transverse momentum (b) Energy (c) Pseudorapidity (d) Azimuthal angle

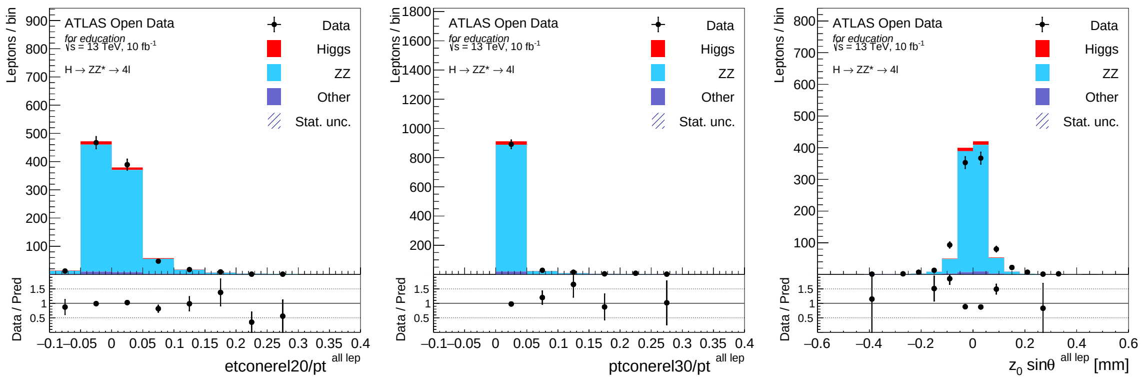

(e) Calorimetric isolation (f) Tracking detector isolation (g) Distance wrt. the p.v.

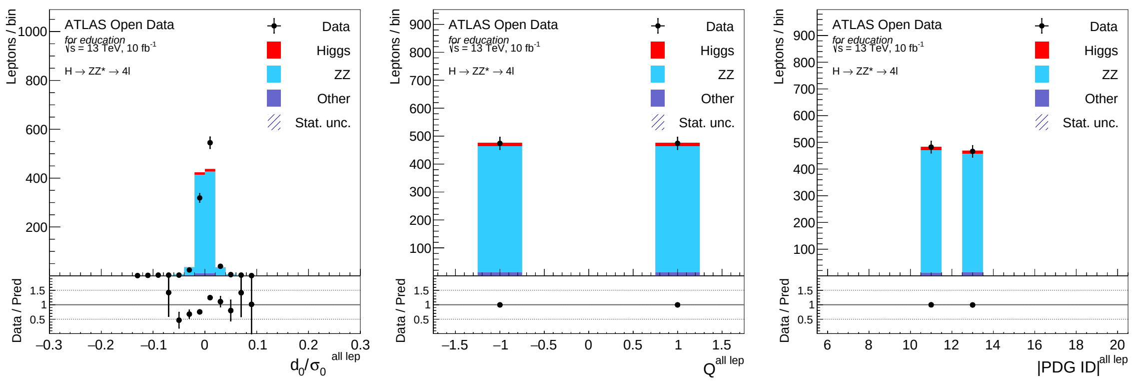

(h) Significance of the track at p.c.a. (i) Lepton charge (j) Lepton type

Figure 2: Comparison between data and MC prediction for the *lepton* variables in the ***4l*** region for the four leptons combined. The lower panels in each figure show the ratio of the data points to the MC histogram simulations. The last bin in all figures contains the overflow. Further details are provided in the text.

5.3 *Global* variables

In Figure 6 the *global* variables in the ***4l*** region are plotted. Again, the distributions in φ are uniform as expected and the agreement between data and MC is generally *good*. The η distributions of $ll1$ and $ll2$ extend to higher values than the ones of leptons or jets in Figures 2 5. This is because, while in the lepton or jet cases a η constraint was added, in the case of bosons no limit on η was requested. The fact that the final state leptons are required to have $|\eta| < 2.5$ doesn't prevent the reconstructed Z to have an η outside these limits. Furthermore, the p_T distributions of $ll1$ and $ll2$ are qualitatively very similar since, for the main processes, each pair originated from a Z boson, which, in turn, originated from a system with low p_T. This causes the Z bosons to have roughly the same p_T. From the number of events in the peak, its width and the lateral tails, it is evident that the invariant mass of $ll1$ is more concentrated around its central value at ~ 90 GeV than the mass of $ll2$. This is because $ll1$ is reconstructed with the SFOS lepton pair with invariant mass closet to m_Z.

On the other hand, the η distribution for the $4l$ system tends to concentrate around $|\eta| \sim 2.5$ and not around zero as all the other distributions so far. This may be caused by the fact that the $4l$ system four-vector is strictly correlated to the primary vertex and so to the elementary interaction of interest. Therefore the distributions of its variables are particularly affected by the production mechanism in question. The distribution in p_T of the the $4l$ system peaks

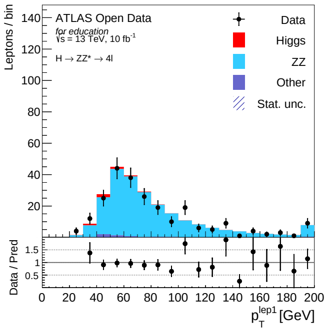

(a) p_T of lepton 1

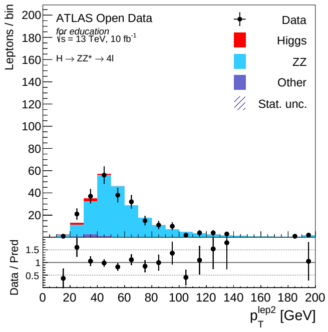

(b) p_T of lepton 2

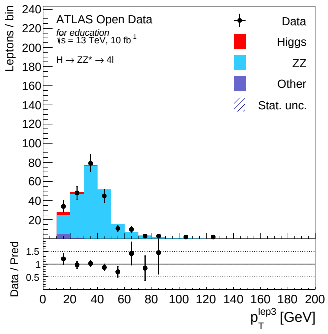

(c) p_T of lepton 3

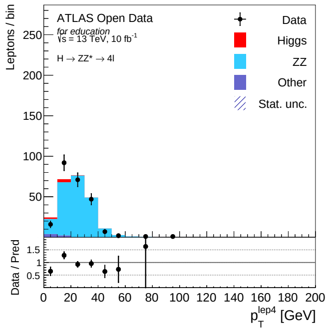

(d) p_T of lepton 4

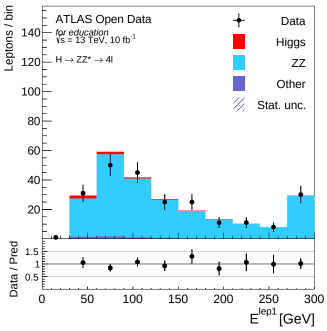

(e) E of lepton 1

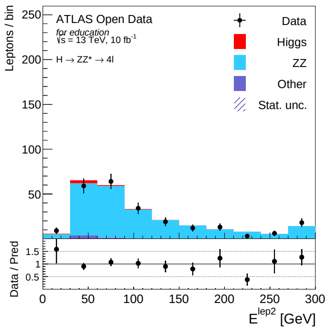

(f) E of lepton 2

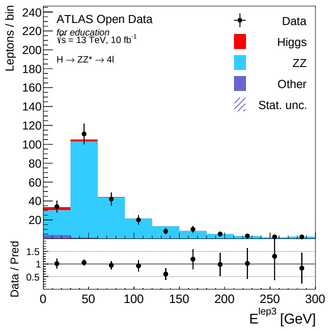

(g) E of lepton 3

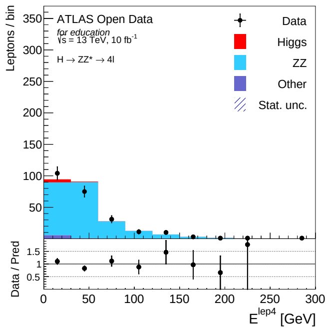

(h) E of lepton 4

Figure 3: Comparison between data and MC prediction for p_T and E in the $\boldsymbol{4l}$ region for leptons 1, 2, 3, 4. The lower panels in each figure show the ratio of the data points to the MC histogram simulations. The last bin in all figures contains the overflow. Further details are provided in the text.

around zero because in the majority of the events there aren't any jets that could balance the p_T. This can be seen clearly in Figure 7, where the p_T in the regions $\boldsymbol{4l+0jets}$, $\boldsymbol{4l+1jets}$ and $\boldsymbol{4l+2jets}$ are plotted. The p_T of the $4l$ system in the events with no jets is concentrated around zero, while the distributions when jets are present tend towards higher values in order to balance such jets. The invariant mass distribution of the $4l$ system has a peak around 125 GeV corresponding to the signal $H \to ZZ^* \to 4l$. Starting at about 180 GeV there is a steep rising in the number of events resulting in a shoulder that continues asymmetrically to very high values. This is caused by the fact that from about 180 GeV two *on-shell* Z bosons can be produced. This distribution can be compared to the m_{4l} one in the ***4l_no_m_lim*** region in Figure 8 in which the constraints on $m_{ll,1}$ and $m_{ll,2}$ vanish. In this case another peak appears around 90 GeV and corresponds to the production of a single Z boson that creates four leptons in the final state. This process consists two steps: first the emission from the Z boson of a γ/Z^*, which in turn decays in a SFOS lepton pair, then the standard decay $Z \to l^+l^-$. If the region with the constraint on $m_{ll,1}$ and $m_{ll,2}$ the peak at about 90 GeV disappears because the process just described is suppressed since the γ/Z^* emitted needs to be above the 12 GeV threshold. Finally, the *global* variables are plotted in Figures 9 and 10 in the ***4e_no_m_lim*** and ***4μ_no_m_lim*** regions respectively.

5.4 *Spin-parity* variables

In order to determine the spin-parity of the Higgs boson, five angles that describe the production (θ^* and Φ_1) and the decay (θ_1, θ_2 and Φ) are defined [5], as show in Figure 11. The three-momentum of the Z_i boson is called $\mathbf{q}_i$, while q_{i1} and q_{i2} indicate respectively the three-momenta of the lepton and anti-lepton associated with Z_i. Indicating as superscript the rest frame in which the three-momenta are taken, the definitions of the angles are:

- $\theta^* \in [0, \pi]$ is the production angle of the leading Z in the four-lepton rest frame

$$\cos\theta^* = \frac{q_{1z}^{4l}}{|\mathbf{q}_1^{4l}|}$$

where q_{1z}^{4l} is the z component of the three-momentum of Z_1 in the four-leptons rest frame

- $\Phi_1 \in [-\pi, \pi]$ is the angle between the decay plane of the leading lepton pair and a plane defined by Z_1 in the four-lepton rest frame and the positive direction of the collision axis $\hat{n}_z = (0, 0, 1)$

$$\Phi_1 = \frac{\mathbf{q}_1^{4l} \cdot (\hat{n}_1 \times \hat{n}_{coll})}{|\mathbf{q}_1^{4l} \cdot (\hat{n}_1 \times \hat{n}_{coll})|} \times \arccos(\hat{n}_1 \cdot \hat{n}_{coll})$$

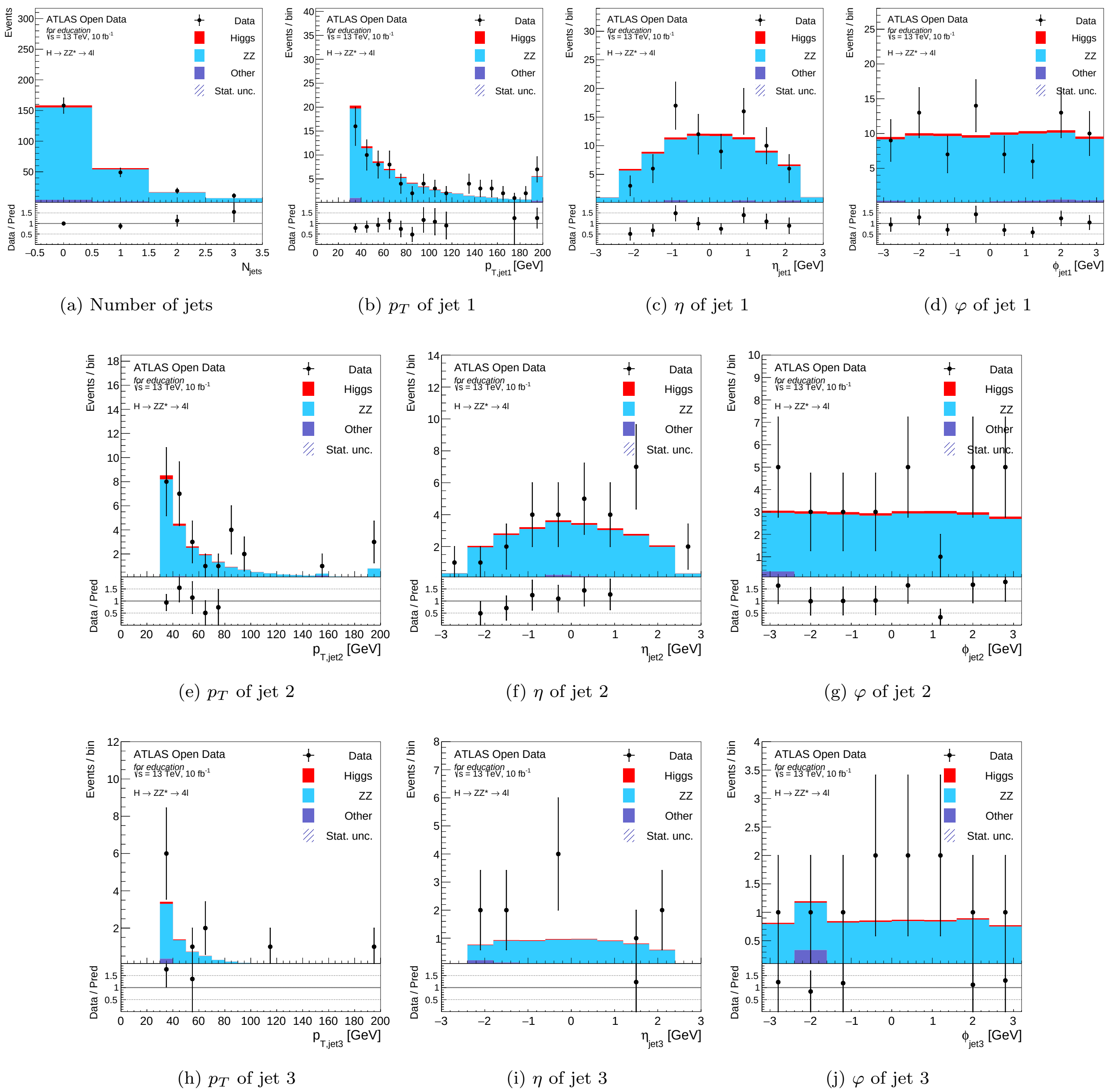

(a) Number of jets (b) p_T of jet 1 (c) η of jet 1 (d) φ of jet 1

(e) p_T of jet 2 (f) η of jet 2 (g) φ of jet 2

(h) p_T of jet 3 (i) η of jet 3 (j) φ of jet 3

Figure 4: Comparison between data and MC prediction for the *jet* variables in the $\boldsymbol{4l}$ region. The lower panels in each figure show the ratio of the data points to the MC histogram simulations. The last bin in all figures contains the overflow. Further details are provided in the text.

where the normal vectors to the two planes are defined as

$$\hat{n}_1 = \frac{\mathbf{q}_{11}^{4l} \times \mathbf{q}_{12}^{4l}}{|\mathbf{q}_{11}^{4l} \times \mathbf{q}_{12}^{4l}|}, \qquad \hat{n}_{coll} = \frac{\hat{n}_z \times \mathbf{q}_1^{4l}}{|\hat{n}_z \times \mathbf{q}_1^{4l}|}$$

- $\Phi \in [-\pi, \pi]$ is the angle between the decay planes of the two lepton pairs in the four-leptons rest frame

$$\Phi = \frac{\mathbf{q}_1^{4l} \cdot (\hat{n}_1 \times \hat{n}_2)}{|\mathbf{q}_1^{4l} \cdot (\hat{n}_1 \times \hat{n}_2)|} \times \arccos\left(-\hat{n}_1 \cdot \hat{n}_2\right)$$

where

$$\hat{n}_2 = \frac{\mathbf{q}_{21}^{4l} \times \mathbf{q}_{22}^{4l}}{|\mathbf{q}_{21}^{4l} \times \mathbf{q}_{22}^{4l}|}$$

- $\theta_1 \in [0, \pi]$ and $\theta_2 \in [0, \pi]$ are the angles between final-state negatively charged leptons and the direction of flight of their respective Z bosons

$$\cos\theta_1 = -\frac{\mathbf{q}_2^{Z_1} \cdot \mathbf{q}_{11}^{Z_1}}{|\mathbf{q}_2^{Z_1}||\mathbf{q}_{11}^{Z_1}|}, \qquad \cos\theta_2 = -\frac{\mathbf{q}_1^{Z_2} \cdot \mathbf{q}_{21}^{Z_2}}{|\mathbf{q}_1^{Z_2}||\mathbf{q}_{21}^{Z_2}|}$$

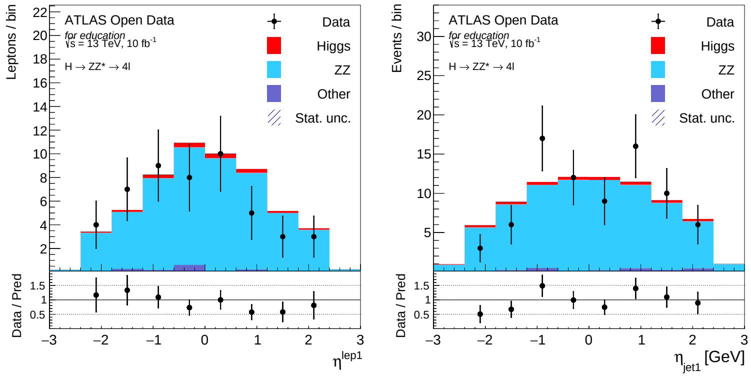

(a) η of lepton 1 (b) η of jet 1

Figure 5: Comparison between data and MC prediction for the η distributions of lepton 1 and jet 1 in the $\boldsymbol{4l + 1jet}$ region. The lower panels in each figure show the ratio of the data points to the MC histogram simulations. The last bin in all figures contains the overflow. Further details are provided in the text.

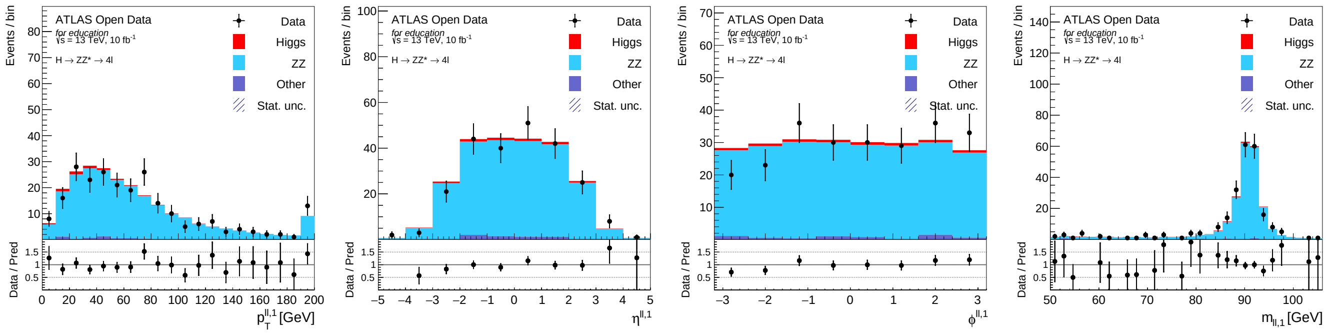

(a) p_T of $ll1$ (b) η of $ll1$ (c) φ of $ll1$ (d) m of $ll1$

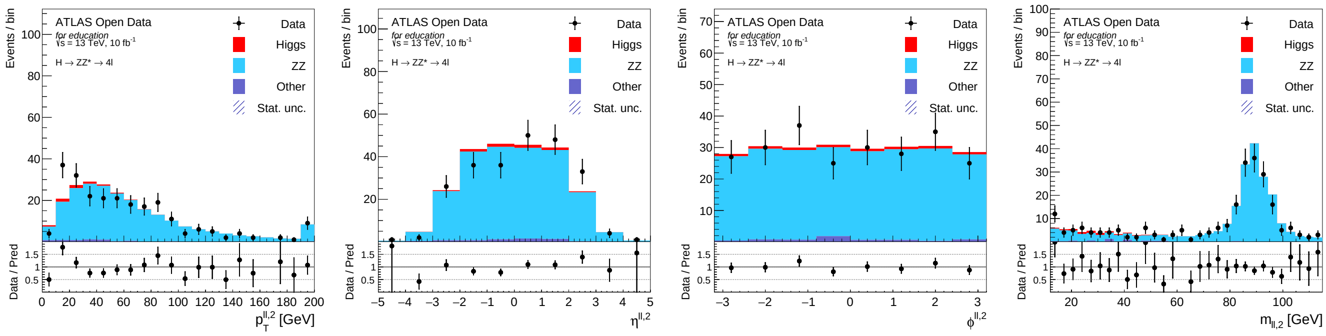

(e) p_T of $ll2$ (f) η of $ll2$ (g) φ of $ll2$ (h) m of $ll2$

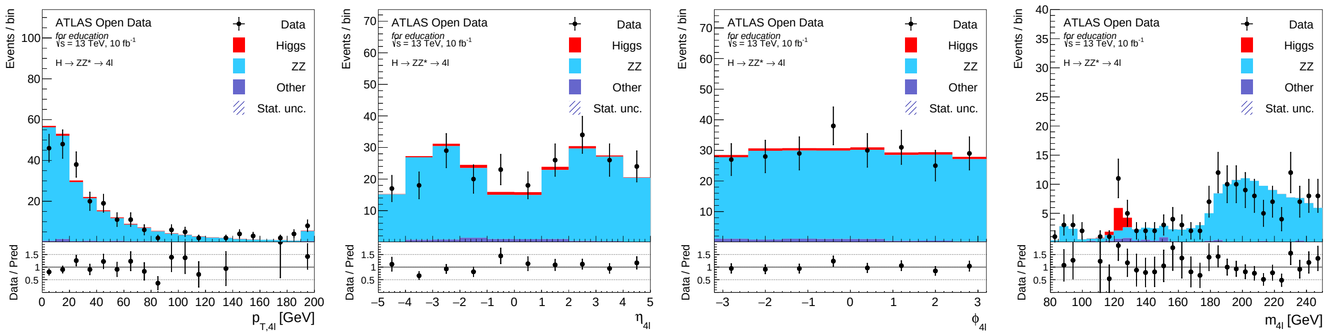

(i) p_T of $4l$ (j) η of $4l$ (k) φ of $4l$ (l) m of $4l$

Figure 6: Comparison between data and MC prediction for the *global* variables in the $\boldsymbol{4l}$ region. The lower panels in each figure show the ratio of the data points to the MC histogram simulations. The last bin in all figures but (l) contains the overflow. Further details are provided in the text.

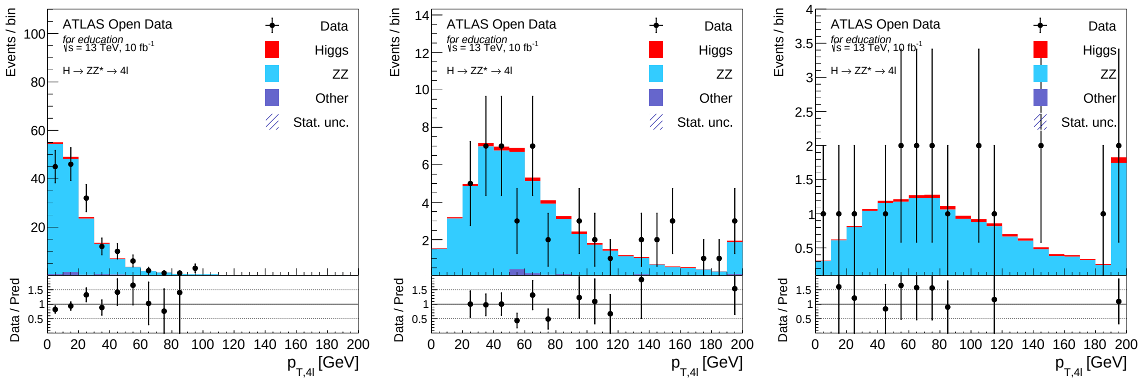

(a) p_T of $4l$ in $\boldsymbol{4l+0jets}$ (b) p_T of $4l$ in $\boldsymbol{4l+1jets}$ (c) p_T of $4l$ in $\boldsymbol{4l+2jets}$

Figure 7: Comparison between data and MC prediction for the p_T of the $4l$ system in the $\boldsymbol{4l+0jets}$, $\boldsymbol{4l+1jets}$ and $\boldsymbol{4l+2jets}$ regions. The lower panels in each figure show the ratio of the data points to the MC histogram simulations. The last bin in all figures contains the overflow. Further details are provided in the text.

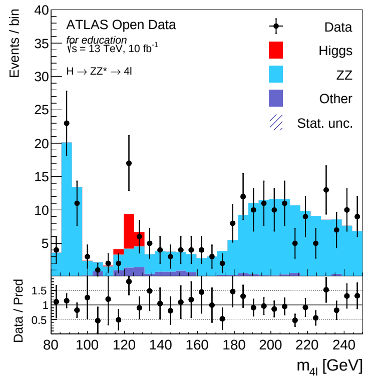

Figure 8: Comparison between data and MC prediction for the invariant mass of the $4l$ system in the $\boldsymbol{4l\_no\_m\_lim}$ region. The lower panels in each figure show the ratio of the data points to the MC histogram simulations. Further details are provided in the text.

In Figure 12 the five angles defined above are plotted in the $\boldsymbol{4l}$ region. In order to increase the signal to background ratio, the same distributions are plotted in the region $\boldsymbol{4l\_m4l\_lim}$ in Figure 13. In the case of a spin-0 boson, the differential production cross section does not depend on the production variables $\cos\theta^*$ and Φ_1 since the initial state doesn't have any preferred directions. In the $\boldsymbol{4l\_m4l\_lim}$ region the signal MC samples are in fact uniform, while in the $\boldsymbol{4l}$ region the $\cos\theta^*$ distribution of the dominant ZZ background tends toward $|\cos\theta^*| \sim 1$. This shows that the non-resonant ZZ are produced preferably in the forward or backward phase space regions in the four leptons system rest frame. There is generally a *good* agreement between data and MC.

The *spin-parity* variables are plotted also in the $\boldsymbol{4e}$ and $\boldsymbol{4\mu}$ regions in Figure 14 and in the $\boldsymbol{ee\mu\mu}$ and $\boldsymbol{\mu\mu ee}$ regions in Figure 15. In the region $\boldsymbol{4e}$ the distribution in $\cos\theta^*$ seems more uniform than the same distribution in the $\boldsymbol{4\mu}$, $\boldsymbol{ee\mu\mu}$ and $\boldsymbol{\mu\mu ee}$ regions. Since θ^* is a variable that describes the production, it shouldn't be affected by the decay channel of the Z boson. This seeming effect may be due to the different η cuts applied to electrons and muons.

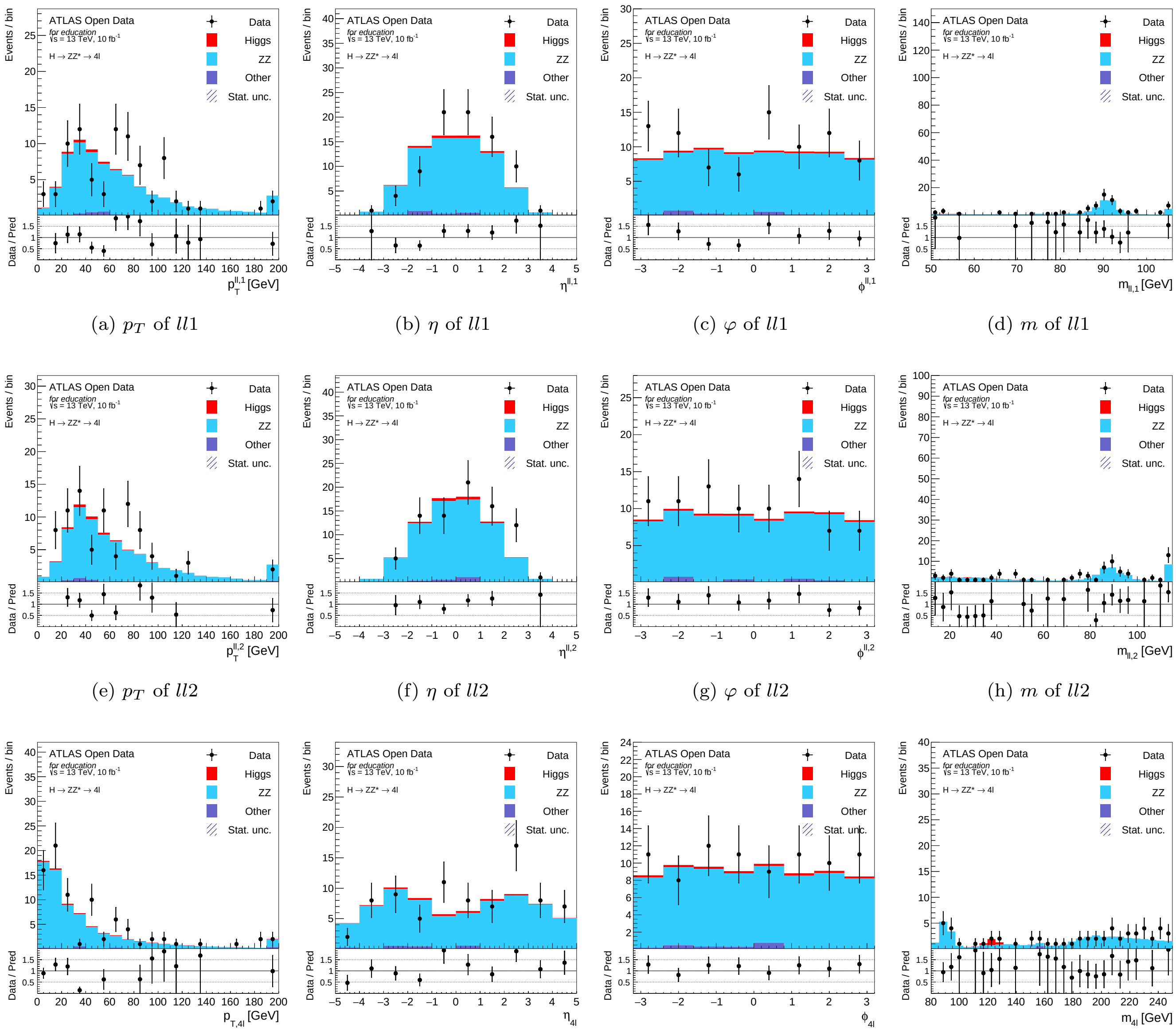

(a) p_T of $ll1$ (b) η of $ll1$ (c) φ of $ll1$ (d) m of $ll1$

(e) p_T of $ll2$ (f) η of $ll2$ (g) φ of $ll2$ (h) m of $ll2$

(i) p_T of $4l$ (j) η of $4l$ (k) φ of $4l$ (l) m of $4l$

Figure 9: Comparison between data and MC prediction for the *global* variables in the ***4e_no_m_lim*** region. The lower panels in each figure show the ratio of the data points to the MC histogram simulations. The last bin in all figures but (l) contains the overflow. Further details are provided in the text.

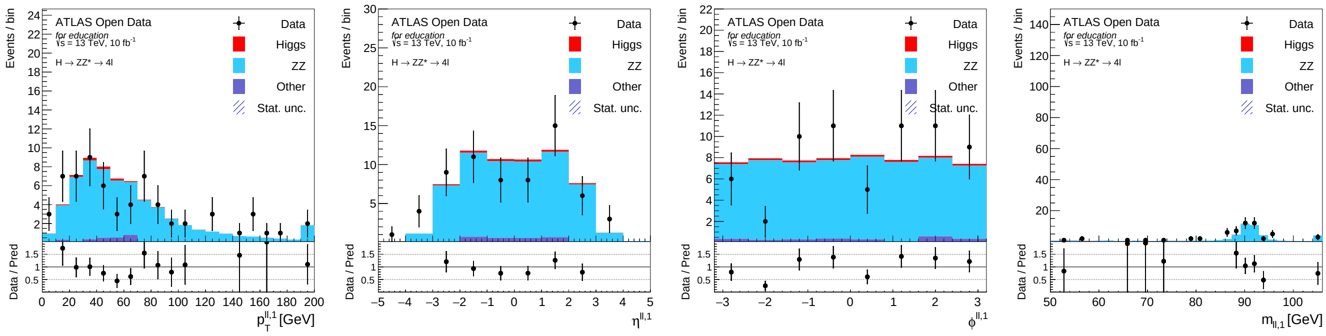

(a) p_T of $ll1$ (b) η of $ll1$ (c) φ of $ll1$ (d) m of $ll1$

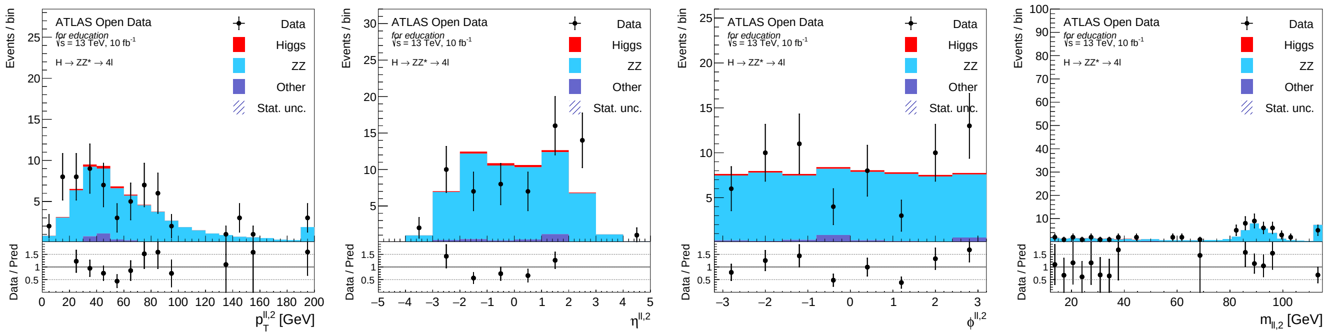

(e) p_T of $ll2$ (f) η of $ll2$ (g) φ of $ll2$ (h) m of $ll2$

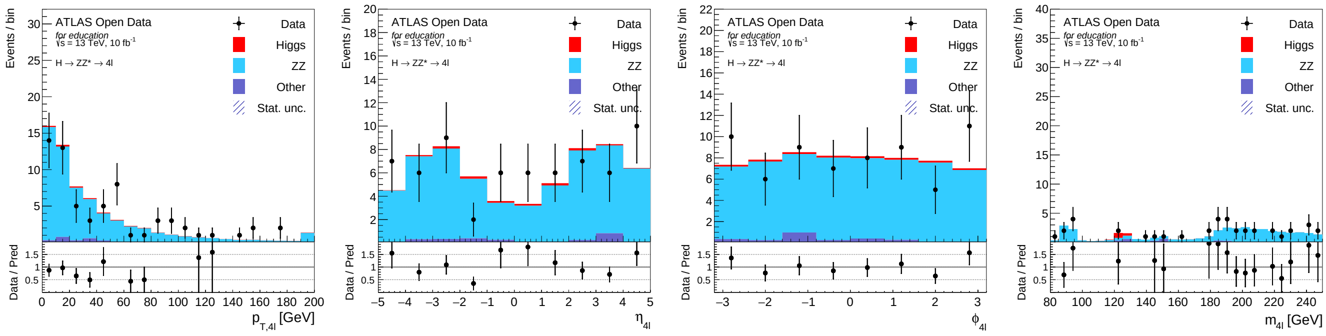

(i) p_T of $4l$ (j) η of $4l$ (k) φ of $4l$ (l) m of $4l$

Figure 10: Comparison between data and MC prediction for the *global* variables in the ***4μ_no_m_lim*** region. The lower panels in each figure show the ratio of the data points to the MC histogram simulations. The last bin in all figures but (l) contains the overflow. Further details are provided in the text.

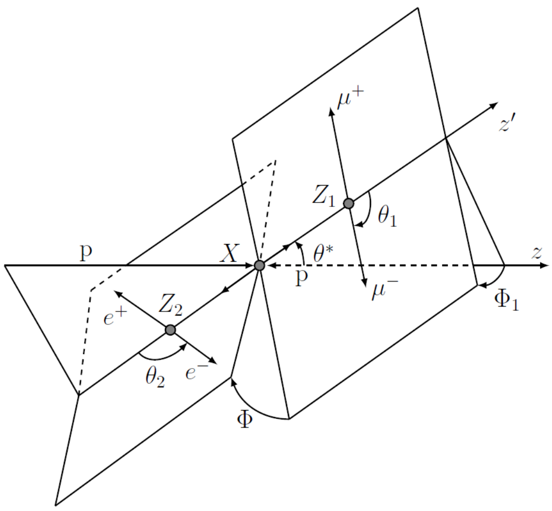

Figure 11: Definition of the angular observables sensitive to the spin-parity of the Higgs boson.

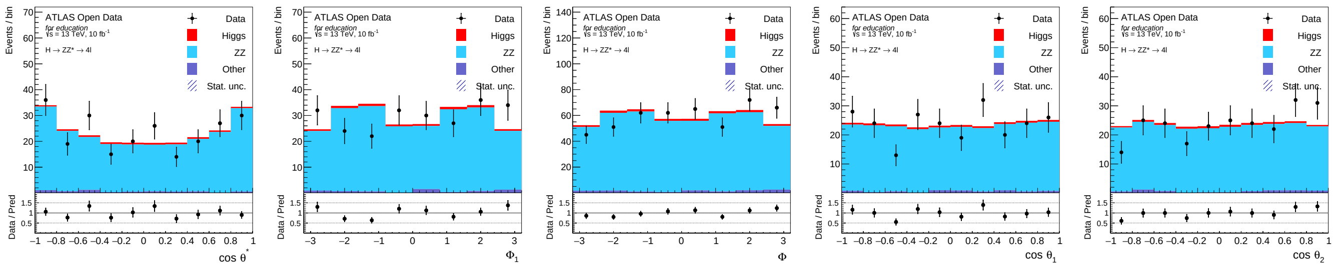

(a) $\cos\theta^*$ (b) Φ_1 (c) Φ (d) $\cos\theta_1$ (e) $\cos\theta_2$

Figure 12: Comparison between data and MC prediction for the *spin-parity* variables in the **4l** region. The lower panels in each figure show the ratio of the data points to the MC histogram simulations. Further details are provided in the text.

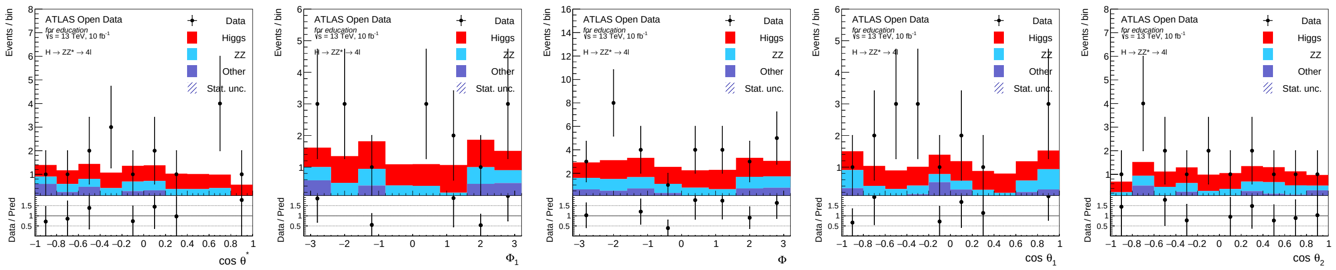

(a) $\cos\theta^*$ (b) Φ_1 (c) Φ (d) $\cos\theta_1$ (e) $\cos\theta_2$

Figure 13: Comparison between data and MC prediction for the *spin-parity* variables in the ***4l_m4l_lim*** region. The lower panels in each figure show the ratio of the data points to the MC histogram simulations. Further details are provided in the text.

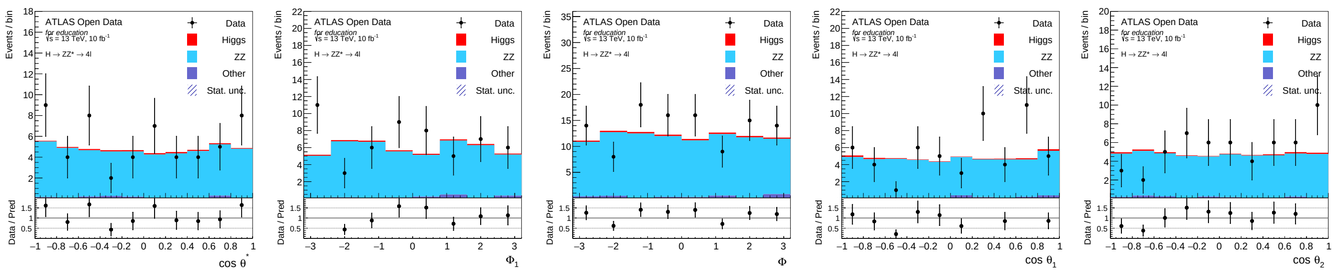

(a) $\cos\theta^*$ in the $\boldsymbol{4e}$ region (b) Φ_1 in the $\boldsymbol{4e}$ region (c) Φ in the $\boldsymbol{4e}$ region (d) $\cos\theta_1$ in the $\boldsymbol{4e}$ region (e) $\cos\theta_2$ in the $\boldsymbol{4e}$ region

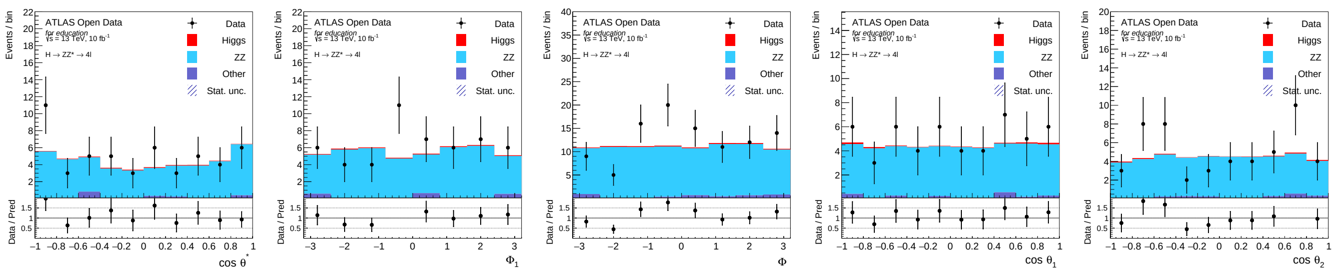

(f) $\cos\theta^*$ in the $\boldsymbol{4\mu}$ region (g) Φ_1 in the $\boldsymbol{4\mu}$ region (h) Φ in the $\boldsymbol{4\mu}$ region (i) $\cos\theta_1$ in the $\boldsymbol{4\mu}$ region (j) $\cos\theta_2$ in the $\boldsymbol{4\mu}$ region

Figure 14: Comparison between data and MC prediction for the *spin-parity* variables in the $\boldsymbol{4e}$ and $\boldsymbol{4\mu}$ regions. The lower panels in each figure show the ratio of the data points to the MC histogram simulations. Further details are provided in the text.

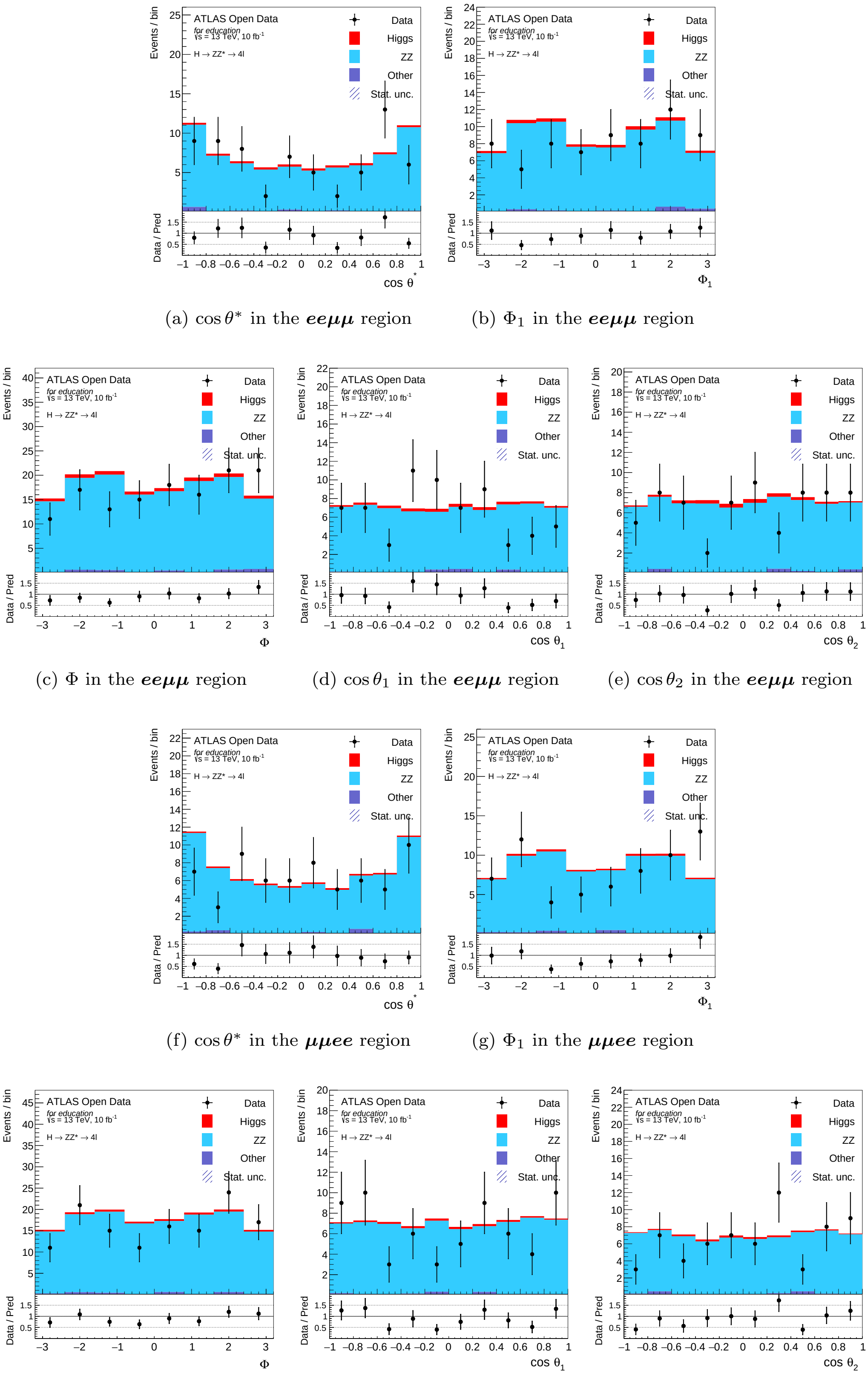

(a) $\cos\theta^*$ in the $\boldsymbol{ee\mu\mu}$ region (b) Φ_1 in the $\boldsymbol{ee\mu\mu}$ region

(c) Φ in the $\boldsymbol{ee\mu\mu}$ region (d) $\cos\theta_1$ in the $\boldsymbol{ee\mu\mu}$ region (e) $\cos\theta_2$ in the $\boldsymbol{ee\mu\mu}$ region

(f) $\cos\theta^*$ in the $\boldsymbol{\mu\mu ee}$ region (g) Φ_1 in the $\boldsymbol{\mu\mu ee}$ region

(h) Φ in the $\boldsymbol{\mu\mu ee}$ region (i) $\cos\theta_1$ in the $\boldsymbol{\mu\mu ee}$ region (j) $\cos\theta_2$ in the $\boldsymbol{\mu\mu ee}$ region

Figure 15: Comparison between data and MC prediction for the *spin-parity* variables in the $\boldsymbol{ee\mu\mu}$ and $\boldsymbol{\mu\mu ee}$ regions. The lower panels in each figure show the ratio of the data points to the MC histogram simulations. Further details are provided in the text.

References

[1] ATLAS Collaboration, *Observation of a new particle in the search for the Standard Model Higgs boson with the ATLAS detector at the LHC*, Phys. Lett. B 716 (2012) 1–29, arXiv:1207.7214 [hep-ex].

[2] CMS Collaboration, *Observation of a new boson at a mass of 125 GeV with the CMS experiment at the LHC*, Phys. Lett. B 716 (2012) 30–61, arXiv:1207.7235 [hep-ex].

[3] ATLAS Collaboration, *Evidence for the spin-0 nature of the Higgs boson using ATLAS data*, Phys. Lett. B 726 (2013) 120–144, arXiv:1307.1432 [hep-ex].

[4] ATLAS Collaboration, *Study of the spin and parity of the Higgs boson in diboson decays with the ATLAS detector*, Eur. Phys. J. C 75, 476 (2015), arXiv:1506.05669 [hep-ex].

[5] S. Bolognesi et al., *On the spin and parity of a single-produced resonance at the LHC*, Phys. Rev. D 86 (2012) 095031, arXiv:1208.4018 [hep-ex].

[6] ATLAS Collaboration, *Electron reconstruction and identification in the ATLAS experiment using the 2015 and 2016 LHC proton–proton collision data at p s = 13 TeV*, Eur. Phys. J. C 79 (2019) 639, arXiv: 1902.04655 [hep-ex]

[7] ATLAS Collaboration, *Muon reconstruction performance of the ATLAS detector in proton–proton collision data at p s = 13 TeV*, Eur. Phys. J. C 76 (2016) 292, arXiv: 1603.05598 [hep-ex]

[8] M. Cacciari, G. P. Salam and G. Soyez, *The anti-kt jet clustering algorithm*, JHEP 04 (2008) 063, arXiv: 0802.1189 [hep-ph]